Supplementary Information

CO Oxidation over Ligand Coordinated Single Site Rh Catalyst: Identification of Active Complex

Fereshteh Rezvani,[1†] Xuemei Zhou,[1,2 †] Debora Motta Meira,[3] George E. Sterbinsky,[4] Steven L. Tait*[1]

[1] Department of Chemistry, Indiana University, 800 E. Kirkwood Ave., Bloomington, Indiana 47405 (U. S. A.), E-mail: tait@indiana.edu

[2] School of Chemical Engineering, Sichuan University, No. 24 South Section 1, Yihuan Road, Chengdu, 610065 (P.R.C.).

[3] Canadian Light Source, Saskatoon, Saskatchewan, Canada.

[4] Advanced Photon Source, Argonne National Laboratory, 9700 South Cass Avenue, Lemont, Illinois 60439 (U.S.A.).

[†] These authors contributed equally to this publication.

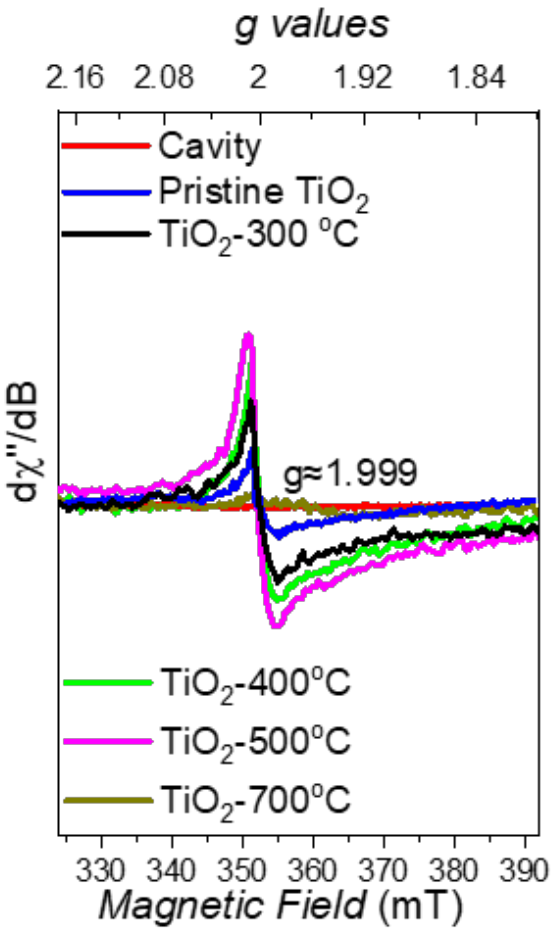

Fig. S1. Solid-state EPR spectra for pristine TiO_2 (blue), and for various degrees of defective TiO_2 prepared by annealing at 300 °C, 400 °C, 500 °C, and 700 °C for 1 h in H_2/N_2. Blank cavity reference shown in red. Figure is reproduced from Zhou, *et al.*,[1] with permission from the Royal Society of Chemistry.

EPR spectra were obtained at room temperature using a Bruker EMX X-band EPR spectrometer. The settings included a microwave frequency of 9.866 GHz, a microwave attenuator set to 15.0 dB, a microwave power of 6.38 mW, a modulation frequency of 100 kHz, and a modulation amplitude of 4.0 G.

We prepared a series of TiO_2 support powders by annealing them at temperatures ranging from 300 °C to 500 °C, to create various surface defect densities. The formation of Ti^{3+}/O_v states in TiO_2 induced by the annealing process was characterized using continuous wave (CW) electron paramagnetic resonance (EPR) spectroscopy. This technique is widely used to analyze

paramagnetic centers, providing signals based on the g tensor, which can distinguish single electrons trapped in regular lattice sites, interstitial sites, or defective sites. Pristine anatase TiO_2 shows a weak signal at a g-tensor value of approximately 2.00 (**Fig. S1**) due to the naturally occurring Ti^{3+}/O_v in commercial anatase TiO_2. For anatase powders annealed between 300 °C and 500 °C, there is a noticeable increase in the intensity of this signal ($g \approx 2.00$), reaching a three-fold increase for anatase annealed at 500 °C. This indicates a higher concentration of Ti^{3+}/O_v sites introduced by annealing in an H_2/N_2 atmosphere.

Several studies have examined the effect of oxygen vacancies on the catalytic activity and reaction mechanism of CO oxidation. It is important to note that most of these studies involve catalysts that are nanoparticles rather than single atom catalysts. For instance, Chen, *et al*., synthesized CuO nanoparticles supported on TiO_2 with a high concentration of oxygen vacancies created through various reduction treatments. This catalyst demonstrated superior catalytic activity compared to CuO supported on pristine TiO_2. DRIFTS experiments showed that the Cu sites are the adsorption sites for CO, and oxygen vacancies can activate O_2 molecules into reactive oxygen species. Regarding the reaction mechanism, they found that the catalyst follows the Mars-van Krevelen (MvK) mechanism.[2] In another study, it was reported that monoatomic oxygen ions (O^-) in oxygen vacancy-rich perovskite $La_{0.8}Sr_{0.2}CoO_3$ catalysts are the primary active oxygen species during the CO oxidation reaction. The researchers demonstrated that molecular oxygen (O_2) is more favorably adsorbed and activated on surface oxygen vacancies through a one-electron transfer process, leading to the formation of O^- species. This significantly enhances low-temperature CO oxidation.[3] In a DFT study by Qi, *et al*., their calculations showed that the presence of oxygen vacancies on the Pd/CeO_2 surface decreases the energy barrier for the CO oxidation reaction. The dissociation of O_2 is facilitated by the oxygen vacancies around the Pd site.[4]

Table S1. Molar ratios of PDO/Rh, Rh/Ti, Cl/Rh, and PDO/Ti from XPS measurements on Rh-PDO/TiO_2, Rh-PDO/def-TiO_2, Rh NPs/TiO_2, Rh-DPTZ/def-TiO_2, and Rh-BPDCA/def-TiO_2. Rh wt.% is measured from ICP-MS. The first three rows of this table are reproduced from **Table 1** for comparison to the bottom two rows.

Catalyst	XPS PDO/Rh mole ratio[a]	XPS Rh/Ti mole ratio	XPS Cl/Rh mole ratio	XPS PDO/Ti mole ratio	ICP Rh wt.%
Rh-PDO/TiO_2	2.31	0.017	0.41	0.039	0.16
Rh-PDO/def-TiO_2	1.14	0.034	0.41	0.038	0.33[b]
Rh NPs/TiO_2	N/A	0.096	0.73	N/A	0.70
Rh-DPTZ/def-TiO_2	1.01	0.015	0.79	0.044	0.07
Rh-BPDCA/def-TiO_2	1.89	0.016	0.60	0.030	0.03

[a] Calculated from XPS N 1*s* peak area and Pt Rh 3*d* peak area.

[b] Rh-PDO/def-TiO_2 with a 1:9 precusror ratio, has 0.22 Rh wt% in ICP-MS.

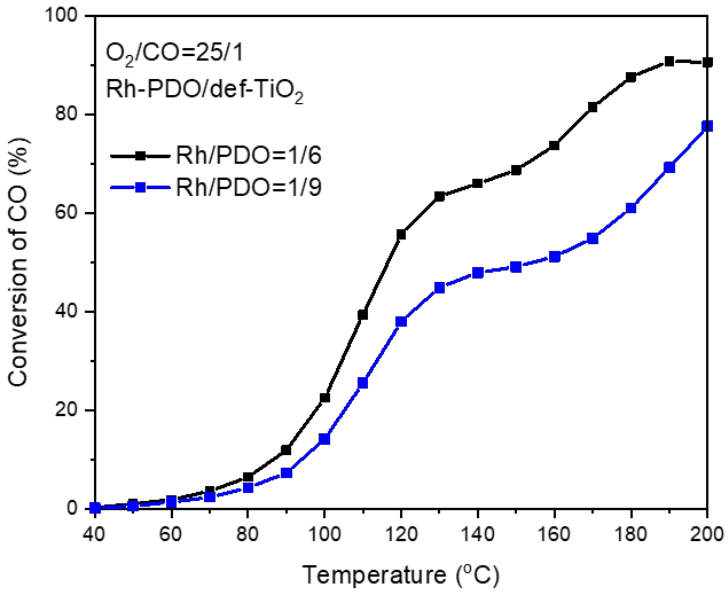

Fig. S2. CO conversion as a function of reaction temperature over Rh-PDO on defective TiO_2 for two samples prepared with Rh:PDO precursor ratios of 1:6 (black curve) or 1:9 (blue curve). With a higher molar ratio of PDO (blue curve), the conversion of CO is slightly lower, but the shape of the conversion curve is similar. The higher loading of the ligand may occupy some of the active sites of Rh.

Table S2. Parameters used for the fitting of EXAFS spectra are shown in **Figs. 6b, S7, S9, and S10**. All samples were analyzed just after synthesis and before running a catalytic reaction, except the samples labeled "post-reaction" were measured after the reaction. Rh-Rh and Rh-O shells were determined from Rh foil and Rh_2O_3 samples, respectively **(Fig. S10 and Table S3)**.

Catalyst	***k* range**	**R range**	**Rh-Cl**			**Rh-N/O**			**Reduced χ^2**	**R factor**
			N	R (Å)	σ^2 (10^{-3})	N	R (Å)	σ^2 (10^{-3})		
Rh-PDO/def-TiO_2	3-14.9	1-3	1.4(± 0.4)	2.33(± 0.01)	2(± 2)	4.8 (± 0.6)	2.03 (± 0.01)	3(± 1)	806	0.014
Rh-PDO/TiO_2	3-13.5	1-3	1.0 (± 0.4)	2.32(± 0.01)	1 (± 2)	5.1 (± 0.6)	2.03 (±0.01)	3 (± 1)	447	0.010
Rh-DPTZ/def-TiO_2	3-14.7	1-3	0.9(± 0.4)	2.33(± 0.01)	2(± 3)	5.2 (± 0.7)	2.02 (±0.01)	4(± 1)	298	0.017
Rh-BPDCA/def-TiO_2	3-13.4	1-3	0.1 (± 0.1)	2.30(± 0.01)	1(± 4)	5.1 (± 0.6)	2.02(± 0.01)	2(± 1)	230	0.014
Rh-PDO/def-TiO_2 (post-reaction)	3-14.8	1-3	1.5(± 0.5)	2.33(± 0.01)	2(± 2)	4.6(± 0.7)	2.03(± 0.01)	3(± 1)	790	0.017
Rh-PDO/TiO_2 (post-reaction)	3-14.7	1-3	1.0(± 0.4)	2.32(± 0.02)	2(± 3)	5.2(± 0.6)	2.03(± 0.04)	3(± 1)	340	0.013
Catalyst	***k* range**	**R range**	**Rh-Rh**			**Rh-N/O**			**Reduced χ**	**R factor**
Rh NPs/TiO_2	3-13.7	1-3	1.7(± 0.9)	2.69(± 0.02)	11 (± 5)	5.2(± 0.4)	2.03(± 0.01)	3(± 1)	1430	0.027
Rh NPs/TiO_2 (post-reaction)	3-14.8	1-3	1.2(± 0.7)	2.69(± 0.03)	10 (± 6)	5.5(± 0.3)	2.03(± 0.01)	3(± 1)	269	0.020

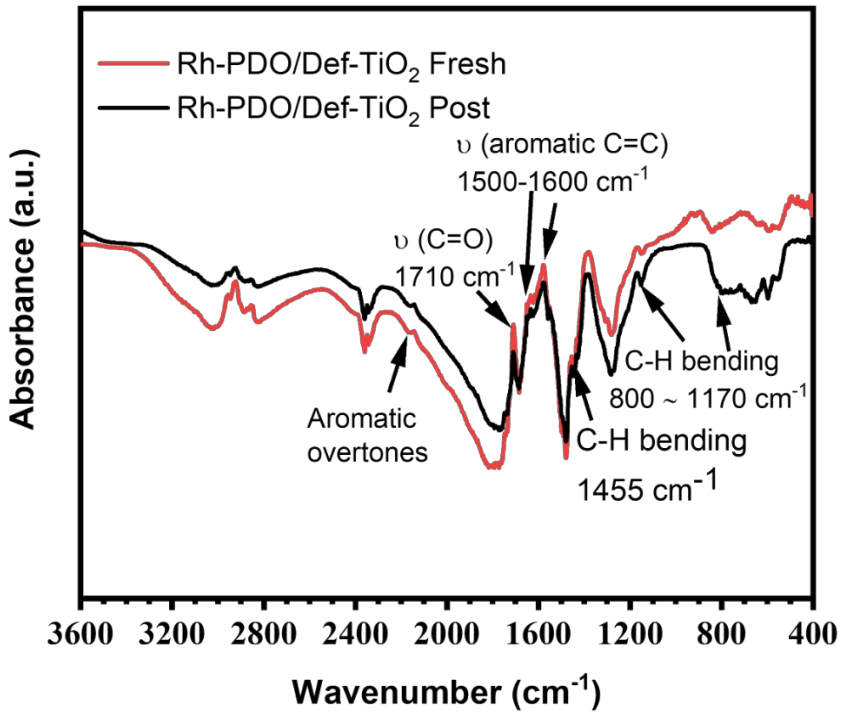

Fig. S3. DRIFT spectra of Rh-PDO/def-TiO_2 as a fresh catalyst (red curve) and after the CO oxidation reaction (black curve). A background spectrum was collected using bare TiO_2. Consistent with XPS results **(Fig. S8)**, these spectra show that the ligand is present on the catalyst before and after the reaction, as indicated by features indicated in the figure. Formate species (2860 cm^{-1} and 2930 cm^{-1}) on TiO_2 show some desorption under reaction conditions.

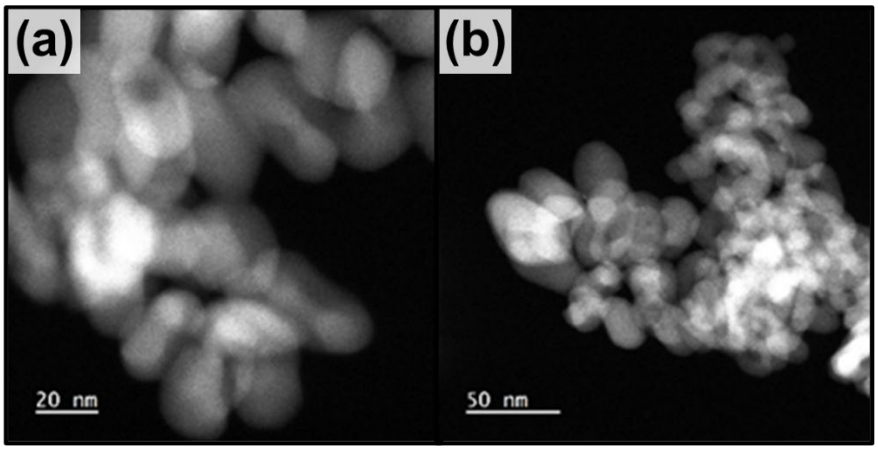

Fig. S4. STEM images of Rh-PDO on pristine TiO_2. No significant Rh nanoparticle formation is observed. These images were obtained with a JEOL JEM 3200FS microscope.

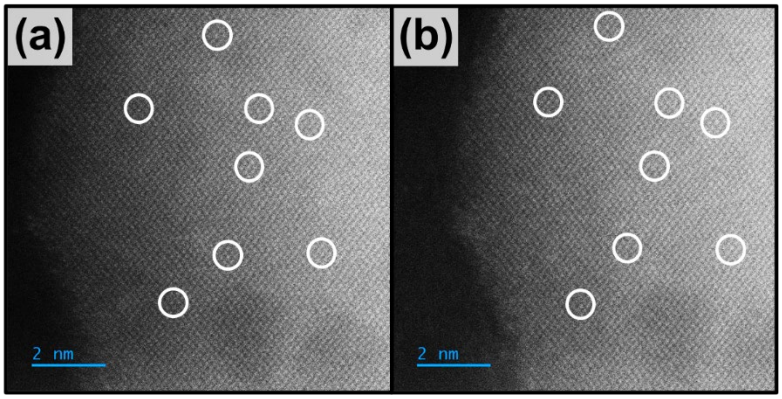

Fig. S5. STEM images of Rh-PDO on defective TiO_2. These two images were recorded subsequently in the same area. Detecting Rh single atoms on a TiO_2 support is expected to be difficult based on prior studies because the atomic number difference is not significant enough for strong contrast. There are several bright features that appear in both images (marked by circles); however, the identification of these features is not clear enough for a thorough analysis. These images were obtained with a JEOL JEM NEOARM microscope.

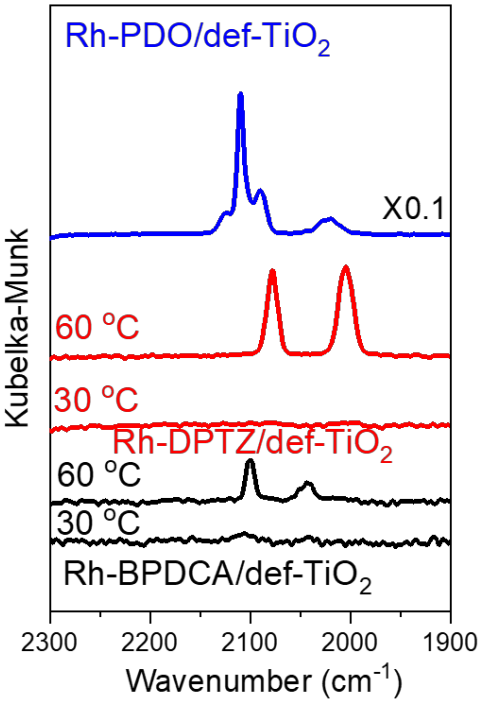

Fig. S6. DRIFT spectra of CO adsorption on Rh-PDO/def-TiO_2 (1:9) at 30 °C, on Rh-DPTZ/def-TiO_2 at 30 °C and 60 °C, and Rh-BPDCA/def-TiO_2 at 30 °C and 60 °C. At 30 °C, there is no CO adsorption on Rh-BPDCA or Rh-DPTZ, but upon heating to 60 °C, some surface species desorb, allowing for adsorption of CO. CO peak positions on Rh-DPTZ (2012 cm^{-1} and 2084 cm^{-1}) indicate $Rh^0(CO)_2$ gem-dicarbonyl species. CO adsorption on Rh-PDO or Rh-BPDCA (2090 cm^{-1} and 2110 cm^{-1}) indicates adsorption on $Rh^{\delta+}$ species. See discussion in the manuscript (section 3.2).

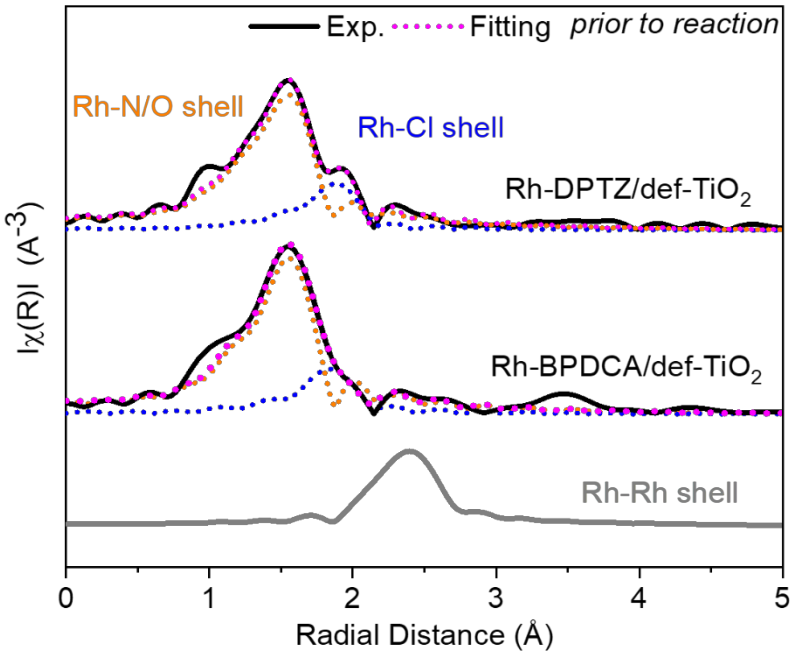

Fig. S7. Fourier transform magnitude of k^2-weighted Rh *K*-edge EXAFS data of Rh-DPTZ and Rh-BPDCA on defective TiO_2 and the fitting result in the first shell. The corresponding fitting data is given in **Table S2**. The results show that no Rh-Rh contribution for the two catalysts.

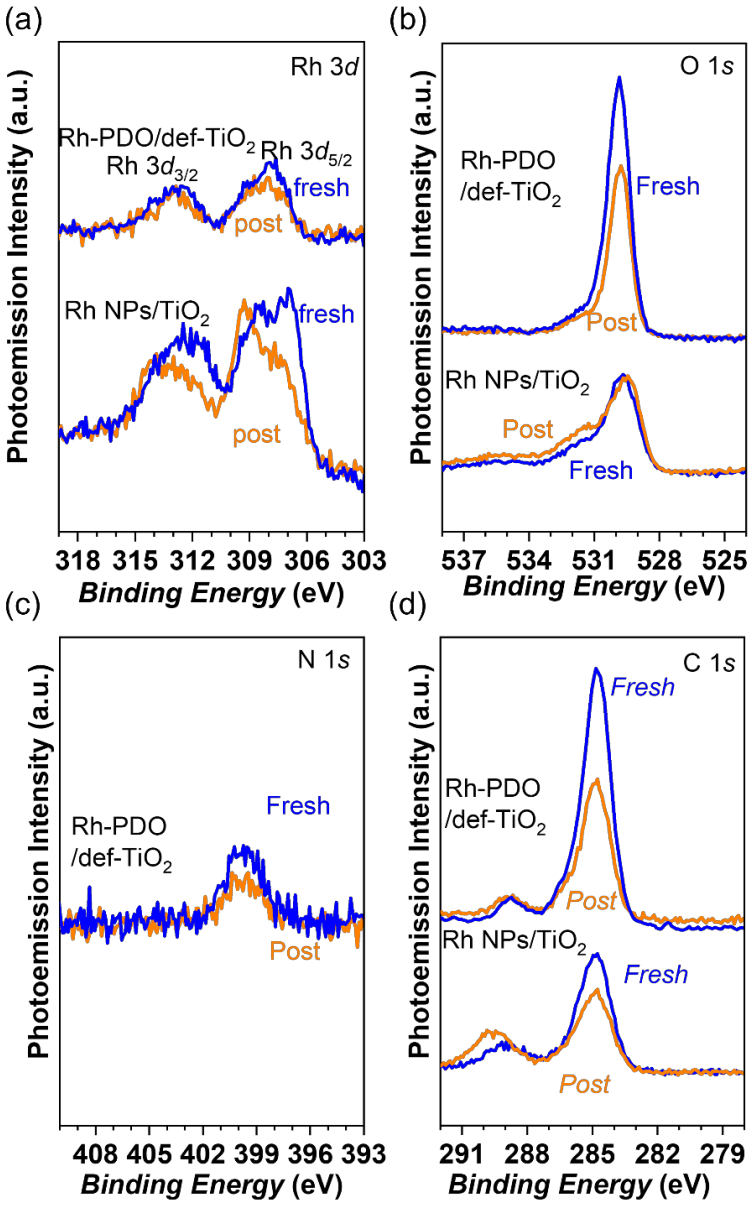

Fig. S8. XP spectra of **(a)** Rh 3*d*, **(b)** O 1*s*, **(c)** N 1*s*, and **(d)** C 1*s* for the fresh (blue curve) and post-reaction catalysts (yellow curve) that include Rh-PDO/def-TiO_2 (top) and Rh NPs/TiO_2 (bottom). Panel (a) presents the same Rh 3d data as in Fig. 10. The O 1*s* spectra (b) show an increased intensity in the shoulder peak at higher BE (*ca.* 532 eV), which belongs to the oxygen species in surface hydroxyls. Although there is some decrease in O and C after the reaction due to the desorption of other surface species, when considered together with the N 1*s* signal (c), the C, N, and O together show the presence of ligand before and after the reaction for Rh-PDO/def-TiO_2 sample. The C 1*s* spectra (d) for Rh NPs/TiO_2 after reaction have shown an increase of peak intensity at higher BE positions (288-291 eV), which may be ascribed to the Rh-carbonate.

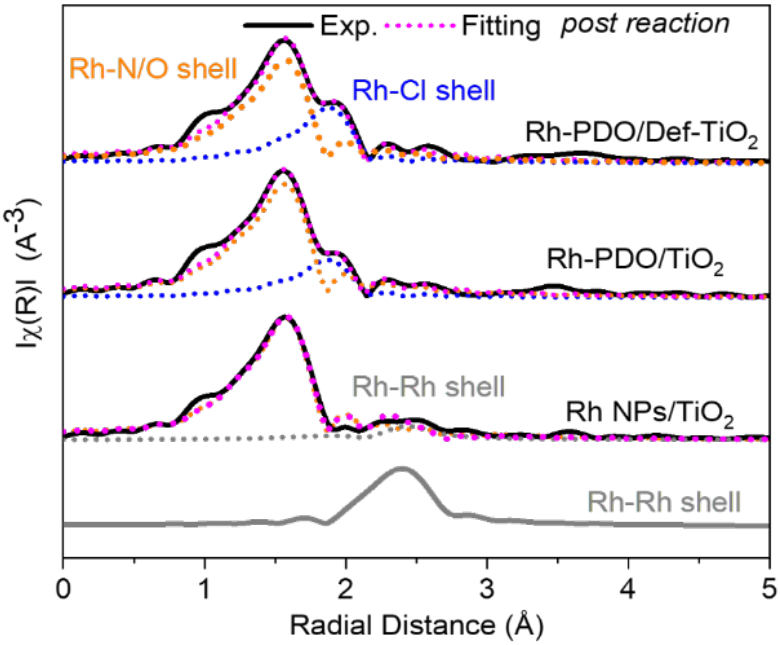

Fig. S9. EXAFS for Rh-PDO/TiO_2, Rh-PDO/def-TiO_2, and Rh NPs/TiO_2 post reactions. These spectra are virtually unchanged from pre-reaction measurements **(Fig. 6b)**.

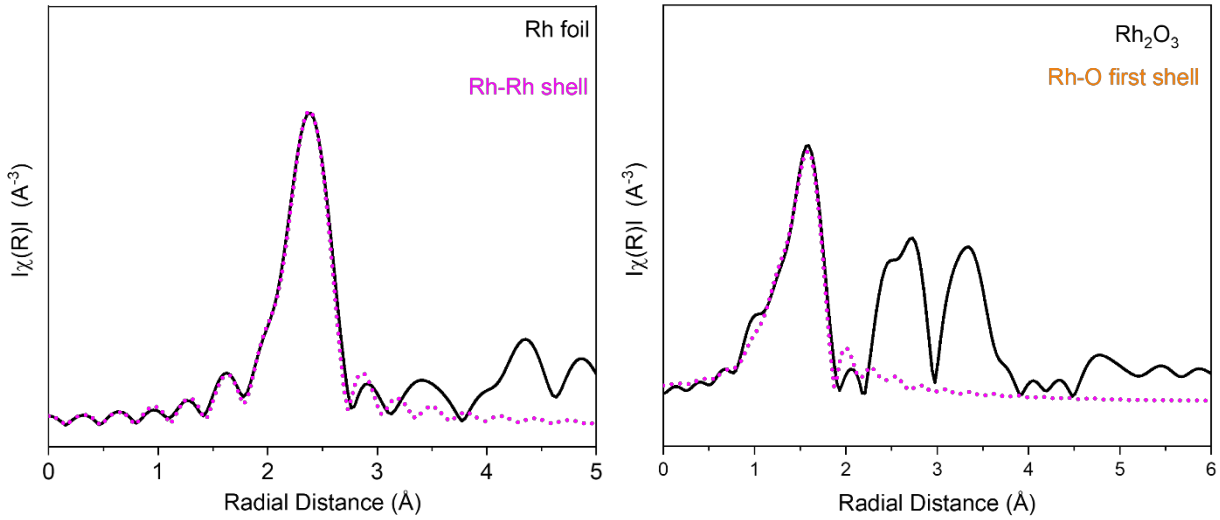

Fig. S10. **(a)** Fourier transform magnitude of k^2-weighted Rh *K*-edge EXAFS data of Rh foil and the fitting result in the first shell. The fitting is carried out using the Rh-Rh path for Rh metal, R_{eff} = 2.689, computed by FEFF. *N* (Rh-Rh) is fixed to be 12. The *k* range is selected between 3-13 Å^{-1} and the *R* range is 1-3 Å. **(b)** Fourier transform magnitude of k^2-weighted Rh *K*-edge EXAFS data of Rh_2O_3 and its fitting result in the first shell. The fitting is carried out using Rh-O path from Rh_2O_3, and *N* (Rh-O) is fixed to be 6. The *k* range is 3-14 Å^{-1} and the *R* range is 1-3 Å. The Rh-O-Rh shell is not considered during fitting. The S_0^2 and ΔE_0 in **Table S3** were used to fit the EXAFS spectra for the catalysts, the results of which are given in **Table S2**.

Table S3. EXAFS fitting parameters for the two Rh standards. The S_o^2 and ΔE_0 were used to fit the Rh-O (first row) path for the Rh-ligand/TiO_2 catalysts (**Table S2**), Rh-O path (first row), and Rh-Rh path (second row) for Rh NPs/TiO_2 without ligand (**Fig. 6**). The *k* range for each of these is 3 –14 Å^{-1}.

Pt standard		**S_0^2**	**ΔE_0/eV**	***R* (Å)**	**σ^2 (10^{-3})**	**Reduced χ^2**	***R*-factor**
Rh_2O_3	Rh-O path	0.8(0.2)	-0.9(3.7)	2.04(0.03)	3 (1)	9083	0.337
Rh foil	Rh-Rh path	0.75(0.06)	-6.8(0.7)	2.69(0.01)	3.4 (0.4)	2384	0.009

References

1. X. Zhou, L. Chen, G. E. Sterbinsky, D. Mukherjee, R. R. Unocic and S. L. Tait, *Catal. Sci. Techno.*, 2020, **10**, 3353-3365.
2. W. Chen, H. Shen, X. Zhu, G. Liu, C. Pan, F. Huang, Y. Fang, Y. Guo and Z. Luo, *Catalysts*, 2022, **13**, 70.
3. J. Yang, S. Hu, Y. Fang, S. Hoang, L. Li, W. Yang, Z. Liang, J. Wu, J. Hu and W. Xiao, *ACS Catal.*, 2019, **9**, 9751-9763.
4. D. Qi, J. Yao, X. Luo and X. Lu, *Chem. pap.*, 2022, **76**, 6975-6983.